





Article

An Auto Adjustable Transimpedance Readout System for Wearable Healthcare Devices

Hyusim Park ¹, Shanthala Lakshminarayana ¹, Chenyun Pan ¹, Hoon-Ju Chung ^{2,*} and Sungyong Jung ^{1,*}

¹ Department of Electrical Engineering, University of Texas at Arlington, Arlington, TX 76019, USA; hyusim.park@mavs.uta.edu (H.P.); shanthala.lakshminarayana@mavs.uta.edu (S.L.); chenyun.pan@uta.edu (C.P.)

² School of Electronic Engineering, Kumoh National Institute of Technology, Gumi 39177, Korea

* Correspondence: hjchung@kumoh.ac.kr (H.-J.C.); jung@uta.edu (S.J.)

Abstract: The objective of this work was to design a versatile readout circuit for patch-type wearable devices consisting of a Transimpedance Amplifier (TIA). The TIA performs Current to Voltage (I–V) conversion, the most widely used technique for amperometry and impedance measurement for various types of electrochemical sensors. The proposed readout circuit employs a digitally controllable feedback resistor (R_f) technique in the TIA to improve accuracy, which can be utilized in a variety of electrochemical sensors within a current range of 0.1 μ A–100 μ A. It is designed to accommodate multiple sensors simultaneously to track multiple target analytes for high accuracy and versatile usage. The readout circuit consists of low power operational amplifier (op–amp) and digital circuit blocks, is designed and fabricated with Magna 0.18 μ m Complementary Metal Oxide Semiconductor (CMOS) technology, which provides low power consumption and a high degree of integration. The design has a small size of 0.282 mm² and low power consumption of 0.38 mW with a 3.3 V power supply, which are desirable factors in wearable device applications.

Keywords: TIA; I–V conversion; CMOS; patch type electrochemical sensing system; healthcare devices



Citation: Park, H.; Lakshminarayana, S.; Pan, C.; Chung, H.-J.; Jung, S.

An Auto Adjustable Transimpedance Readout System for Wearable Healthcare Devices. *Electronics* **2022**, *11*, 1181. <https://doi.org/10.3390/electronics11081181>

Academic Editor: Anna Richelli

Received: 7 March 2022

Accepted: 5 April 2022

Published: 8 April 2022

Publisher's Note: MDPI stays neutral with regard to jurisdictional claims in published maps and institutional affiliations.



Copyright: © 2022 by the authors. Licensee MDPI, Basel, Switzerland. This article is an open access article distributed under the terms and conditions of the Creative Commons Attribution (CC BY) license (<https://creativecommons.org/licenses/by/4.0/>).

1. Introduction

Wearable devices have emerged as powerful tools for environmental examination, healthcare devices, and motion recognition, despite some challenges such as miniaturization and low power while ensuring accuracy, that limit their widespread applicability as continuous monitoring systems of target information [1–3]. Especially with the current trend in an acceleration of global population aging, one-third of the population has been reported to be over 60 years of age in most regions by 2050, resulting in a high demand for healthcare wearable devices [4]. Since the immune response declines with age, the elderly might suffer from many more health risks, which requires healthcare workforces [5]. The wearable devices could be used to address some of the challenges related to detecting and managing adverse health conditions in aging populations, and to reducing ubiquitous healthcare issues [6,7]. As the demand for wearable devices for healthcare continues to rise, it has generated a booming market, and the companies are now seeing the opportunities of supplying wearable healthcare technologies to their consumers as beneficial. So far, wristwatches, gloves, patches, headbands, eyeglasses, and necklaces have been reported as types of wearable devices [8–16]. The wristwatch is the most affordable and widely invented wearable device type since it can provide good wearing comfort and obtain information from the skin. At the same time, it does not require flexibility other than the wristband part, which indicates that commercial-off-the-shelf (COTS) can be utilized as components to build readout circuits for interpreting sensors' information. As a result, we can find watch type of commercial products easily available in the market, such as the Apple Watch (Apple Inc., Cupertino, CA, USA), Fitbit (Fitbit, San Francisco, CA, USA), Samsung Galaxy Watch (Samsung Electronics, Suwon, Korea), and so on. Those mentioned

commercial products show positive effects to improve people's life quality and reduce the potential emergency situation; however, they have limitations as healthcare devices since they are mainly focused on motion recognition utilizing accelerometer and gyroscope to track physical activities, not electrochemical sensors or biosensors which can diagnose or sense symptoms of disease from the body. The mentioned limitation makes them not suitable for accurate and multifunctional healthcare devices. For example, in the case of stress, which is considered a source of many types of illness, a watch type stress monitoring device is not able to perform a comprehensive stress analysis since it can only measure skin conductance [15].

Recent research studies in the sensor field have explored various wearable sensors for monitoring electrophysiological signals and bio-analytes [17–21]. Epidermal materials provide classes of skin-mounted sensors in physical formats that enable intimate, conformal contact with the skin. The soft, non-irritating nature of this contact yields an interface that simultaneously provides high precision and high accuracy measurement of biophysiological parameters, such as temperature, hydration, strain, and biopotential. Such epidermal sensors are ultrathin, breathable, and stretchable, with mechanical and thermal properties that closely match to the skin itself to enable effective skin integration with minimum constraints on natural processes [18,19]. Not limited to developing single target wearable flexible sensors, the latest studies are trying to adopt multifunctional sensors in a single platform [17,18,20,21]. For instance, one research group reported a multifunctional sweat-based electrochemical physiological hybrid skin patch for precise glucose detection in sweat with pH and temperature correction and simultaneous monitoring of electrocardiogram (ECG) [20]. However, only a few of the complete patch type devices have been reported due to the constraints on readout circuits. The readout circuits can be implemented using COTS or Integrated Circuit (IC). Generally, the COTS is preferred in most of the readout circuits for wearable devices since it is easily accessible, so that less time is required to prove the concept. However, readout circuit comprised of COTS is not suitable as patch type of the device since it is not flexible nor miniaturized. Especially, if the readout circuit needs to deal with multiple sensors, the burden increases because it requires more COTS components. Therefore, to avoid utilizing COTS components, devices consist of a sensor and a Radiofrequency (RF) antenna, where sensor output is voltage since an RF antenna can only transfer voltage information [22]. In other works, if patch type of the healthcare device's sensor output is a current, only sensor validation is conducted with test equipment through external wires [17,21]. Therefore, the I–V converter designed in IC for multiple sensors is required to build a complete patch type of the healthcare device. Moreover, the IC is not only offering miniaturization but also shows better accuracy than the COTS.

Herein, we report a versatile and wide ranged I–V converter circuit for multiple patch type of sensors which is fabricated using the Complementary Metal Oxide Semiconductor (CMOS) process. It can accommodate five sensors, which can be expandable; its measurable sensor current range is 0.1 μA to 100 μA , which is chosen based on the practical sensor output current range [23–25]. The rest of this paper is organized as follows. Section 2 describes the specifications and design of the proposed readout circuit. Then, Section 3 discusses simulation and IC test results. Finally, the conclusion is drawn in Section 4.

2. Design of Readout Circuit

Several high-performance current measurement circuit topologies are discussed in [26–41]. One of the common architectures for low current measurements is based on an integrator followed by a differentiator [34–36]. This structure provides a high gain and linear response at the cost of a low dynamic range of about 5 decades and takes a long time to accumulate the small current into a measurable voltage signal. Moreover, the integrator is prone to saturation and requires either additional DC current offset compensation or an active reset switch. Another well-known architecture is a logarithmic I–V converter, which works on the principle of compression of the input signal and utilizes an exponential device as a feedback element in the Transimpedance Amplifier (TIA) [27–29]. Although the logarithmic amplifier

can provide a very wide dynamic range, it often comprises linearity of the output response. Furthermore, it is accompanied by a significant temperature sensitivity and nonlinearity that are difficult to address without the use of an additional temperature compensation circuit. Few other current measurement circuits rely on capacitive TIA (C-TIA) to perform current-to-frequency (I-F) conversion [33]; timed integrators with a switched capacitor network or correlated double sampler [37–41]; variable gain amplifiers with external voltage control or digital gain control [26,31,32]; and use of large feedback resistor realized as an on-chip active pseudo resistor or off-chip external resistor. In the case where a pseudo resistor is realized using a transistor, the resistance is inversely proportional to the input current, which leads to a variable current gain and bandwidth that is undesirable. Among all these architectures, the simple and straightforward approach is a shunt feedback amplifier, based on a voltage inverting amplifier with a feedback resistor (R_f), also called the resistive TIA (R-TIA) [35,42–44] but suffers from a relatively low dynamic range. Here, the R_f directly affects the dynamic range of the TIA, and if it is employed to measure low current, the R_f must be large enough to obtain high gain. Thus, there is a trade-off between achieving high dynamic range and performing low current measurement, which can be resolved using a variable R_f . In this paper, an I-V converter with a digitally controlled programmable gain is proposed to obtain different gain settings to vary the transimpedance gain as a function of the input signal range. The programmable current gain setting enables to achieve a higher overall input dynamic range. Figure 1 illustrates a conventional R-TIA which consists of an operational amplifier (op-amp) with a R_f . In this configuration, a single R_f is connected between an inverting input and output pin of the op-amp [45].

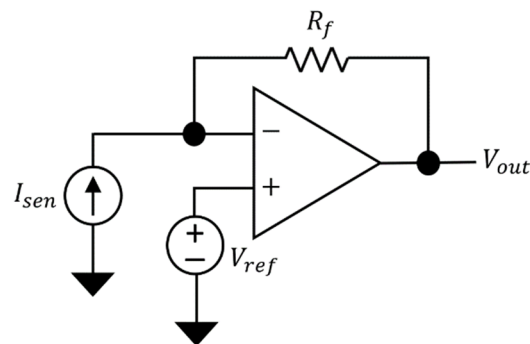


Figure 1. Circuit of conventional resistive Transimpedance Amplifier (R-TIA).

The voltage output (V_{out}) of this configuration can be obtained as

$$V_{out} = -\left(I_{sen} \times R_f\right) + V_{ref} \quad (1)$$

where I_{sen} indicates a sensor current output, V_{ref} is a reference voltage for biasing the op-amp, and V_{out} is voltage obtained at the TIA output. Thus, by measuring the V_{out} , the unknown value of I_{sen} can be calculated by Equation (1). It is important to select the appropriate value of the R_f to obtain an accurate sensor output in the R-TIA configuration, and a digitizing process is essential to process sensor output. If the value of the R_f is too large, the V_{out} will be clipped due to the op-amp output swing limitation, while if the value of the R_f is too small, the V_{out} is not sufficiently large enough to be detected by an Analog-to-Digital Converter (ADC), which is also related to the resolution of the ADC. For instance, when the R_f is fixed to 10 k Ω , to differentiate between 1 μ A and 0.91 μ A, the ADC should be able to interpret the 0.9 μ V difference based on Equation (1) which is challengeable. Meanwhile, if the R_f is set to 100 k Ω , the op-amp output is clipped when I_{sen} is 100 μ A, due to the op-amp's output swing limitation. Thus, the R-TIA with digitally adjustable R_f controlled by a Microcontroller Unit (MCU) is developed in this work to resolve the discussed issues. Based on the V_{out} range, the R_f value will be altered by the

MCU automatically to avoid the clipping problem and the situation that the V_{out} difference is going below the ADC's detectable voltage.

The readout circuit is designed to accommodate five sensors with a current range from 0.1 μA to 100 μA in a single platform. The target error rate is less than 1% while ensuring minimized size and power consumption. The proposed design is implemented using Magna 0.18 μm CMOS technology to provide an optimal performance between the power consumption and the speed. The technology uses 3.3 V as a power supply, provides a resistor with 2% tolerance, and offers a pad with a size of 60 $\mu\text{m} \times 60 \mu\text{m}$ for external connection.

2.1. Design of Digitally Adjustable TIA

A block diagram of the proposed readout circuit is shown in Figure 2, where the I_{sen} indicates each sensor's current output. The circuit consists of an analog multiplexer (AMUX), digitally adjustable TIA, and inverting amplifier. At the input of the circuit, a 5×1 AMUX is implemented to interface with five sensors in a single chip. The heart of the proposed readout circuit is a digitally adjustable R-TIA, which is embarked for accurate and wide-ranged I-V conversion. It is comprised of an op-amp and a digitally controlled feedback stage for varying the R_f to cover a wide sensor current range. The feedback stage includes an 8×1 AMUX and a resistor array containing eight different resistors. Since the R-TIA output is inverted, an additional inverting amplifier is embedded at the last stage to obtain the positive V_{out} . An external MCU, "FreeSoC2 development board" (Cypress Semiconductors, San Jose, CA, USA) is utilized to control the selection bits ($S_0 \sim S_5$) of the AMUXs by general purpose input/output (GPIO) pins. The V_{out} is converted to digital form using an internal 16-bit sigma-delta ADC integrated into the MCU.

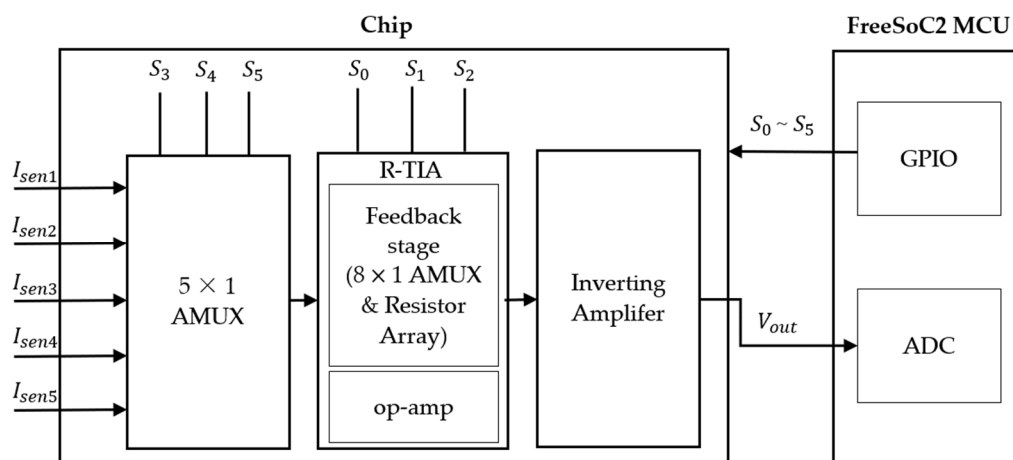


Figure 2. Block diagram of the proposed readout.

2.1.1. OP-AMP Design

A two-stage op-amp comprising of a bias stage, differential amplifier stage, and common source amplifier stage is designed, as shown in Figure 3. The two-stage op-amp topology usually has the advantage of high gain, high linearity, high output swing, low noise, and good bandwidth. The differential gain stage is introduced, where M_1 forms differential pair with M_2 and a current mirror (M_7, M_8), as the first stage of the op-amp. The minimum transistor length used in the design is 1 μm and the differential transistor pair (M_1, M_2) width is chosen as 32 μm . A differential input signal applied across the two input terminals (V^-, V^+) will be amplified according to the gain of the differential stage. By utilizing current mirror active load transistors (M_7, M_8), it can have a very large output impedance. The second stage is consisted of M_5 and M_6 transistors with size of 220 μm and 120 μm , respectively, which is a common source amplifier for high output swing as the final stage amplifier [42,46]. The transistor pair (M_3, M_4) is designed as 42 μm and all the

remaining transistor widths are selected as 15 μm . The cascode current source technique has been implemented to reduce the voltage variations across current source transistors, thus, it can provide accurate current [47]. The first stage gain of the designed op-amp can be represented using Equation (2).

$$A_1 = -g_{m1} (r_{o2} || r_{o7}) \tag{2}$$

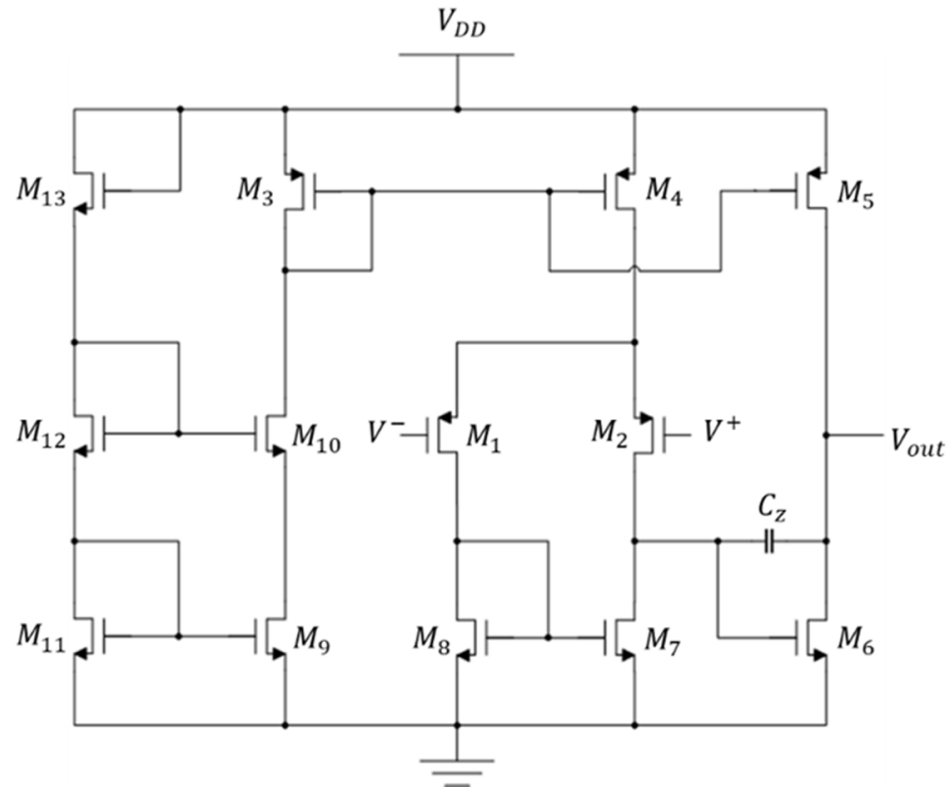


Figure 3. Schematic of the designed operational amplifier (op-amp).

The second stage gain can be expressed as per Equation (3).

$$A_2 = -g_{m6} (r_{o6} || r_{o5}) \tag{3}$$

By combining Equations (2) and (3), the total gain of the designed op-amp can be described as

$$A_{total} = A_1 \times A_2 = g_{m1} g_{m6} (r_{o2} || r_{o7}) (r_{o6} || r_{o5}) \tag{4}$$

Figure 4 shows the op-amp gain and phase plot during the simulation. For biasing the op-amp, V_{ref} of 1.65 V is given to M_2 . The op-amp achieves a 97.5 dB gain and 64.05 degrees phase margin as depicted in Figure 4.

2.1.2. Feedback Stage Design

The feedback stage is made up of an 8×1 AMUX and resistor array, which includes 10 K Ω , 50 K Ω , 100 K Ω , 200 K Ω , 400 K Ω , 600 K Ω , 800 K Ω , and 1 M Ω resistors. The AMUX is connected in a series with the resistor array to vary the R_f by controlling the selection bits of the AMUX, as shown in Figure 5. Each of the I_{in} in Figure 5 indicates the sensor output current (I_{sen}) that passed through the R_f in the resistor array. Depending on the current range of the sensor, the R_f value will be altered to avoid the op-amp output swing limitation or accuracy issue due to the ADC resolution. Table 1 shows the sensor current range and the matched value of R_f , as per the AMUX selection bits (S_2, S_1, S_0).

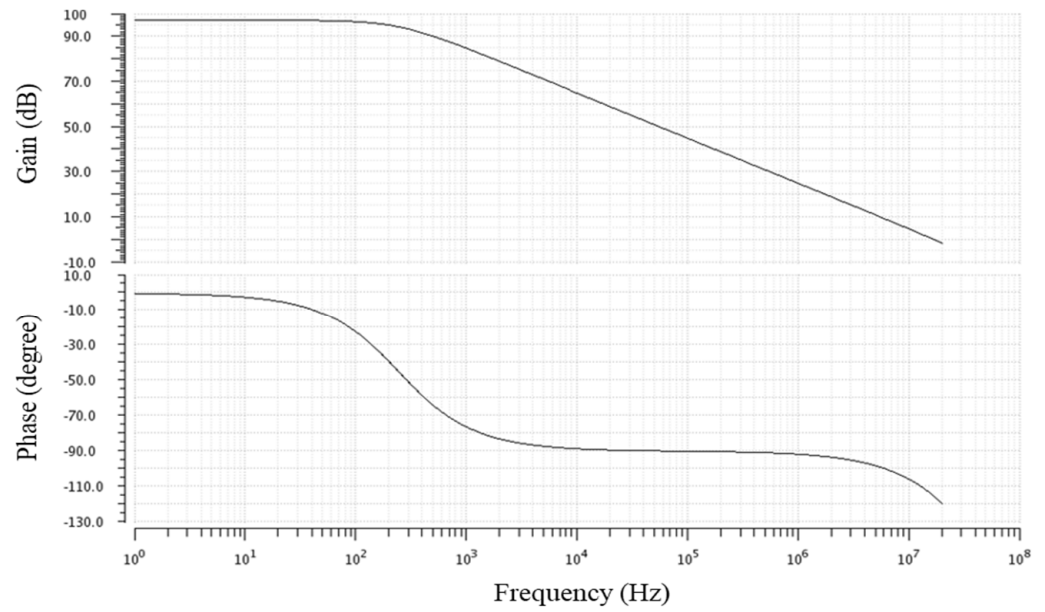


Figure 4. Op-amp gain and phase plot.

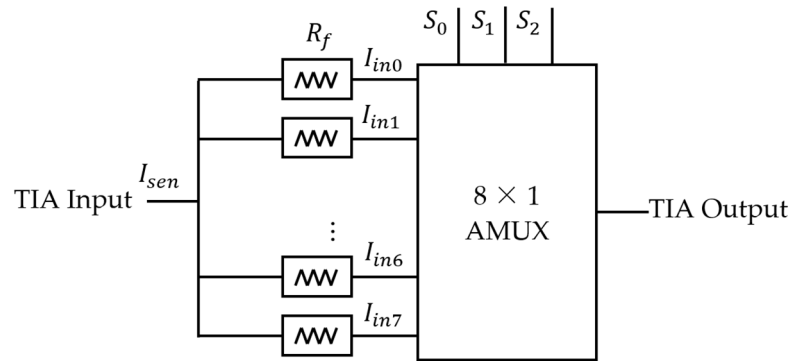


Figure 5. Block diagram of the feedback stage.

Table 1. Feedback resistor selection with sensor current range.

S_2	S_1	S_0	Feedback Resistor R_f (K Ω)	Sensor Current Range I_{sen} (μ A)
0	0	0	10	32~100
0	0	1	50	12~32
0	1	0	100	8~12
0	1	1	200	4~8
1	0	0	400	2.5~4
1	0	1	600	2~2.5
1	1	0	800	1.5~2
1	1	1	1000	0.1~1.5

The AMUX is a combinational logic circuit designed to switch one of the several analog input lines through to a single common output line and is controlled by the selection bits. The designed AMUX is composed of: (a) Combinational logic acting as a decoder for the selection bits; and (b) Transmission Gates (TG) for transferring signal from input to output. The combinational logic for decoder is realized with NOT gates and three input NAND gates. The TG, also called as analog switch, can selectively block or pass a signal from its

input to output. The TG is comprised of a p-channel metal-oxide semiconductor (PMOS) transistor and a n-channel metal-oxide semiconductor (NMOS) transistor pair. The utilized gates' schematics are illustrated in Figure 6. The control gate of TG is biased by the control signal in a complementary manner, so both transistors are either on or off. The decoder output ($d_0 \sim d_7$) is connected to the control signal of the NMOS transistor, and the inverted decoder output ($\overline{d_0} \sim \overline{d_7}$) is connected to the control signal of the PMOS transistor. An output expression (Out) of the AMUX is represented in Equation (5) and the full schematic of the AMUX is presented in Figure 7.

$$\text{Out} = I_{in0}(\overline{s_2} \overline{s_1} \overline{s_0}) + I_{in1}(s_2 \overline{s_1} \overline{s_0}) + I_{in2}(\overline{s_2} s_1 \overline{s_0}) + I_{in3}(s_2 s_1 \overline{s_0}) + I_{in4}(\overline{s_2} \overline{s_1} s_0) + I_{in5}(s_2 \overline{s_1} s_0) + I_{in6}(\overline{s_2} s_1 s_0) + I_{in7}(s_2 s_1 s_0) \tag{5}$$

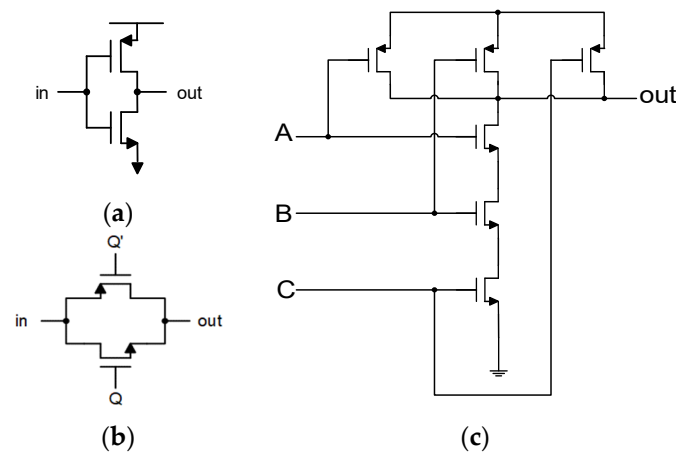


Figure 6. Schematic of (a) NOT gate; (b) Transmission Gate (TG); (c) NAND gate.

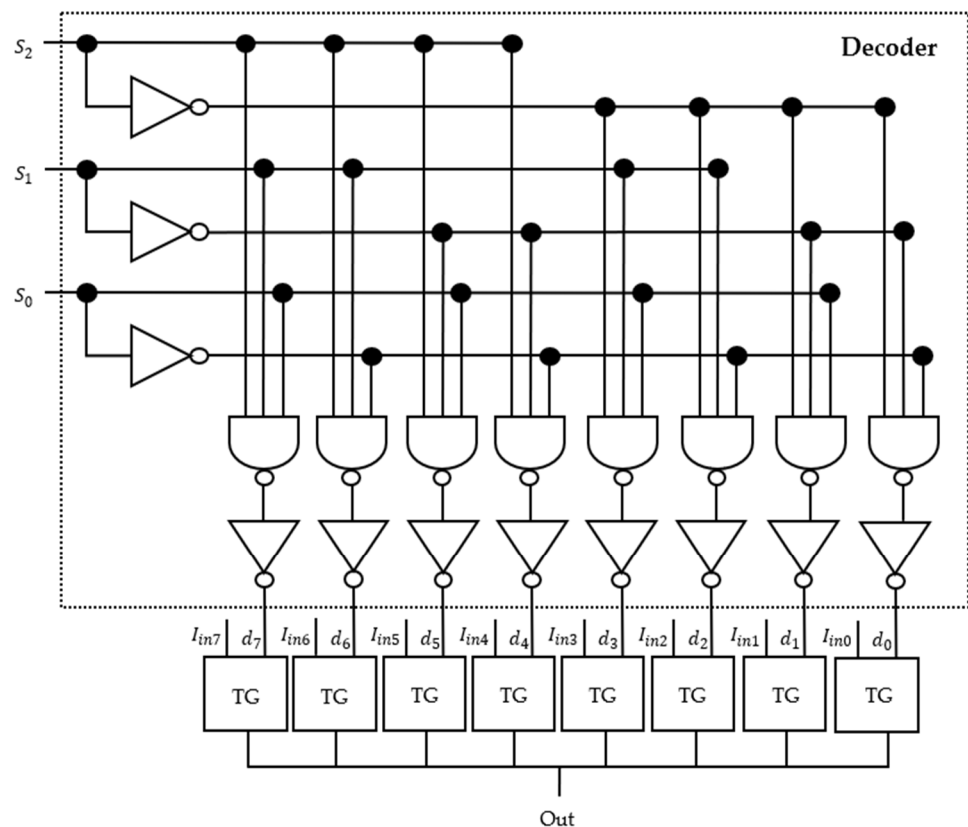


Figure 7. Schematic of an analog multiplexer (AMUX).

3. Results and Discussion

3.1. Simulation Results

The proposed readout circuit shown in Figure 2 is designed in CMOS 0.18 μm technology utilizing the “Cadence” tool (Cadence Design Systems, San Jose, CA, USA). Figure 8a shows the layout of the complete chip, and Figure 8b illustrates the layout of the proposed architecture, which is the circuit marked as ‘A’ in Figure 8a. The designed circuit occupies an area of $1030 \times 620 \mu\text{m}^2$, including the pads and $580 \times 487 \mu\text{m}^2$, excluding the pads. Figure 9 shows the photo of the fabricated chip. In order to verify the proposed circuit, post simulation of the R-TIA has been conducted. As an example, the simulations were plotted in Figure 10 where R_f is 10 K Ω , 100 K Ω , and 1 M Ω , respectively, which cover the minimum and the maximum target range. The Y-axis of the graph in Figure 10 indicates V_{out} in unit of volts, while the X-axis represents I_{sen} in units of μA . The I_{sen} ranges used for simulations are selected based on Table 1, which are from 32 μA to 100 μA ; 8 μA to 12 μA ; and 0.1 μA to 1.5 μA when R_f values are 10 K Ω , 100 K Ω , and 1 M Ω . The results are well matched with the expected results, which are calculated by Equation (1) and show a linear response throughout the dynamic range. The result demonstrated that the proposed circuit could read signals accurately from electrochemical or biosensor where its current output is within the range 0.1 μA to 100 μA . With the variable R_f , the TIA achieved a variable 3 dB bandwidth in the range 3.235 KHz to 225 KHz. Moreover, the TIA exhibits a phase margin of 134.9° , 134.8° , and 126° , when R_f is 1 M Ω , 100 K Ω , and 10 K Ω , respectively. Thus, the designed TIA shows a phase margin higher than 45° with all R_f values in Table 1 indicating the stability of the TIA.

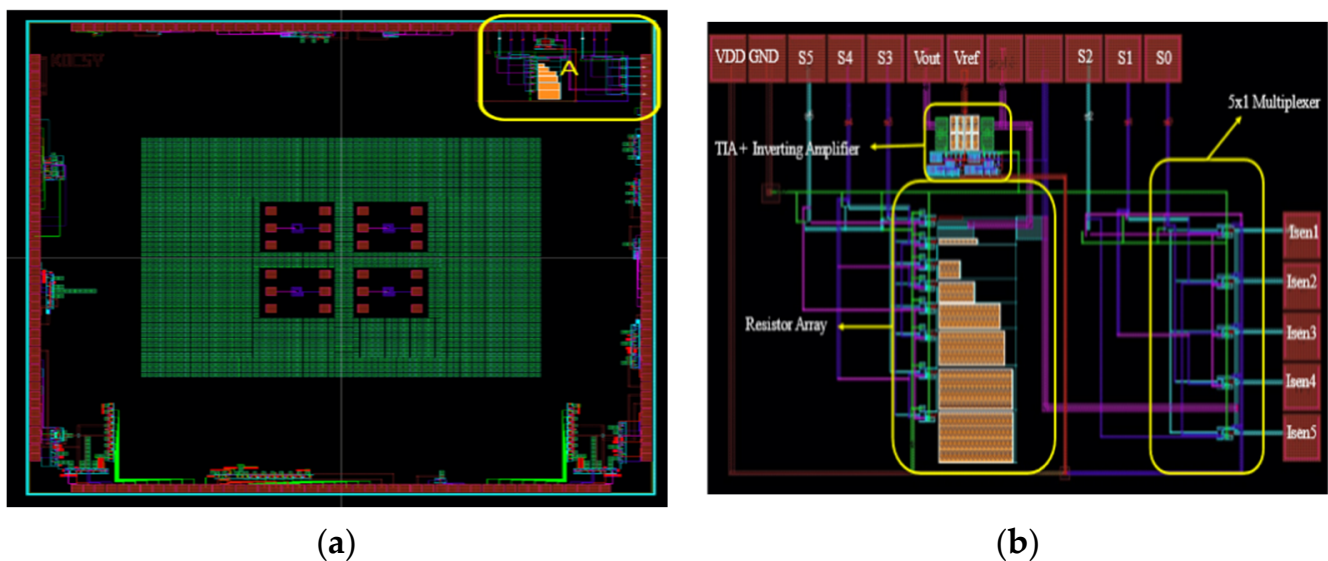


Figure 8. (a) Layout of the fabricated chip; (b) layout of the proposed readout circuit.

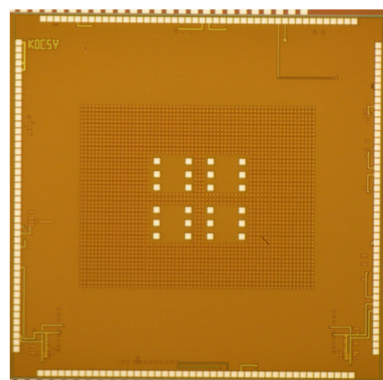
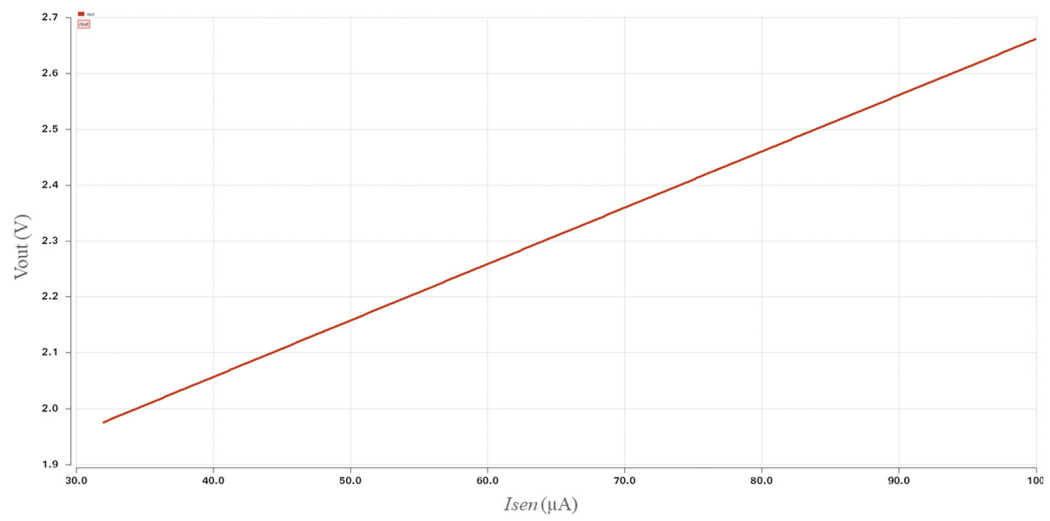
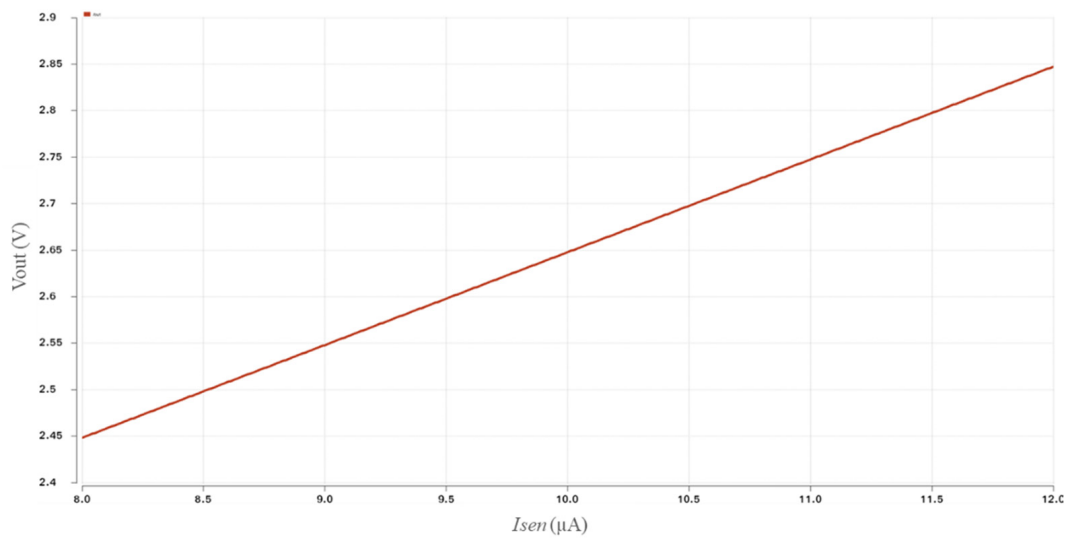


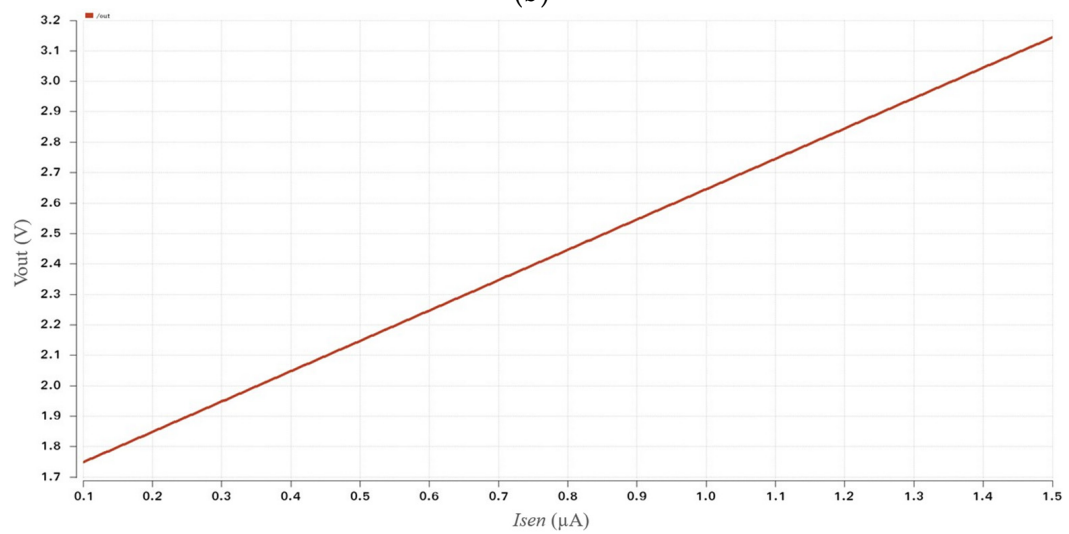
Figure 9. Photo of the fabricated chip.



(a)



(b)



(c)

Figure 10. Simulation results illustrating the voltage output (V_{out}) versus sensor current (I_{sen}) with different feedback resistors (R_f) (a) $R_f = 10\text{ K}\Omega$; (b) $R_f = 100\text{ K}\Omega$; (c) $R_f = 1\text{ M}\Omega$.

3.2. IC Test Results

The fabricated chip is packaged with a quad flock package in order to test the chip, and the chip socket is soldered onto an adapter board. The chip is then inserted inside the socket and tested. Figure 11 illustrates the block diagram of the experimental test setup. An “Agilent power supply” (Keysight Technologies, Santa Rosa, CA, USA) is connected to the V_{DD} pin (3.3 V) and the V_{ref} pin (1.65 V) to power the circuit. To measure the V_{out} , a 16-bit sigma-delta ADC embedded in the “FreeSoC2 development board” is utilized. A 16-bit ADC should be able to differentiate 50 μV difference when V_{DD} is 3.3 V. However, the last two or three bits are generally not trustable due to the error from non-ideal characteristics of the ADC, environmental condition, and offset voltage [48]. Thus, a 16-bit ADC can differentiate 400 μV difference in general. An 8-bit Current Digital to Analog Converter (IDAC) implemented in the MCU is connected to the input of the chip to generate and sweep the I_{sen} for testing the chip. The range of the IDAC in the “FreeSoC2 development board” can be chosen between 2040 μA with an 8 μA resolution and 255 μA with a 1 μA resolution or 31.873 μA with a 0.125 μA resolution. The target current range of this work is from 0.1 μA to 100 μA . Thus, IDAC current ranges of 255 μA with a 1 μA resolution and 31.873 μA with a 0.125 μA resolution were selected as I_{sen} for testing purpose.

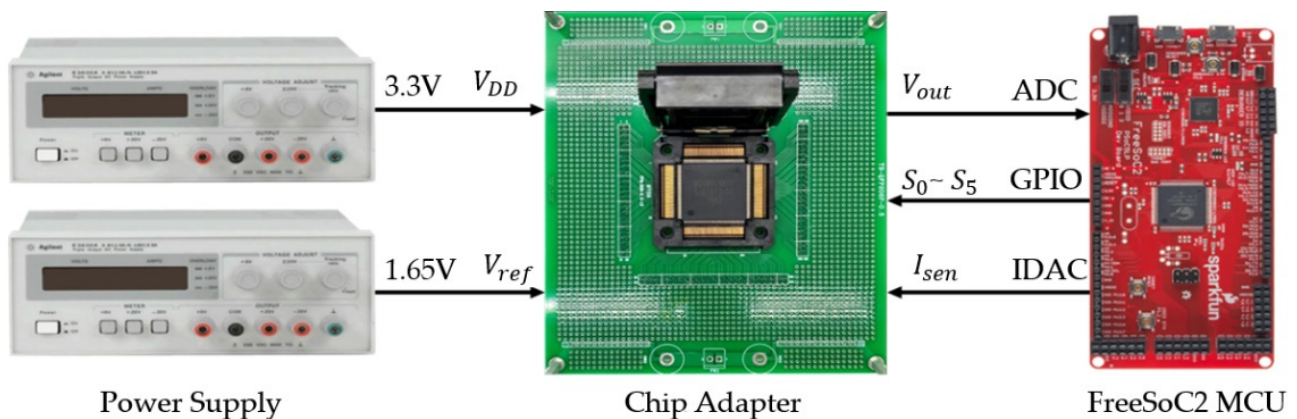


Figure 11. Block diagram of the experimental test setup.

In this work, an algorithm has been developed in the MCU firmware, which can alter the R_f automatically, depending on the I_{sen} range. Figure 12 explains the firmware flowchart of the algorithm. Initially, the R_f values are stored in the MCU memory. Once the MCU is on, it selects the AMUX selection bits (S_2, S_1, S_0) as (1, 1, 1), which indicates that R_f is 1 M Ω and starts to read the ADC voltage. To avoid the clipping issue due to the op-amp output swing limitations, if the ADC value is larger than 3.2 V, it alters the R_f with a smaller value until the R_f reaches 10 K Ω . If not, the MCU calculates the I_{sen} value using Equation (1). With this developed firmware, the R_f of the R-TIA can be changed automatically depending on the I_{sen} range, so that the proposed circuit can cover a wide current range of the sensor.

The comparison of the post simulation results and the measurement results during the IC test experiment are recorded in Figure 13, which shows a linear V_{out} versus I_{sen} from 0.1 μA to 100 μA for different values of R_f . The error in Figure 13 was calculated by below Equation (6)

$$Error (\%) = \frac{V_{measured} - V_{post\ simulation}}{V_{post\ simulation}} \times 100 \quad (6)$$

where the $V_{measured}$ is the measured voltage at the ADC and $V_{post\ simulation}$ is the voltage obtained from post simulation. Figure 13 demonstrates an adequately similar output with a slight offset because of the R_f error, due to the process resistance tolerance of 2 %, which is fairly linear and can be corrected using the offset correction in the MCU. Thus, the

proposed circuit designed in IC is verified that it can cover a wide sensor current range from 0.1 μA to 100 μA . The error rate comparison between the conventional R-TIA with the fixed R_f and proposed R-TIA with digitally adjustable R_f is conducted and presented in Table 2. For comparison, the R_f of the conventional R-TIA is fixed to 10 K Ω , while the R_f in the proposed design is altered based on the I_{sen} range. The measured I_{sen} in Table 2 are extracted from calculation based on Equation (1). In the case where I_{sen} is 100 μA , since both methods are using the same R_f value, they exhibit a similar error rate. However, when the I_{sen} is getting smaller, the proposed TIA shows a much better error rate than the conventional R-TIA, as illustrated in the comparison results in Table 2.

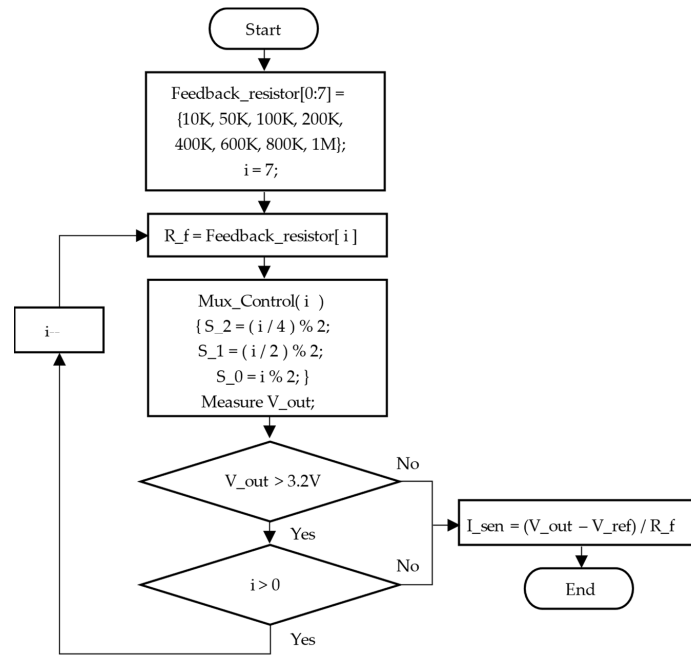
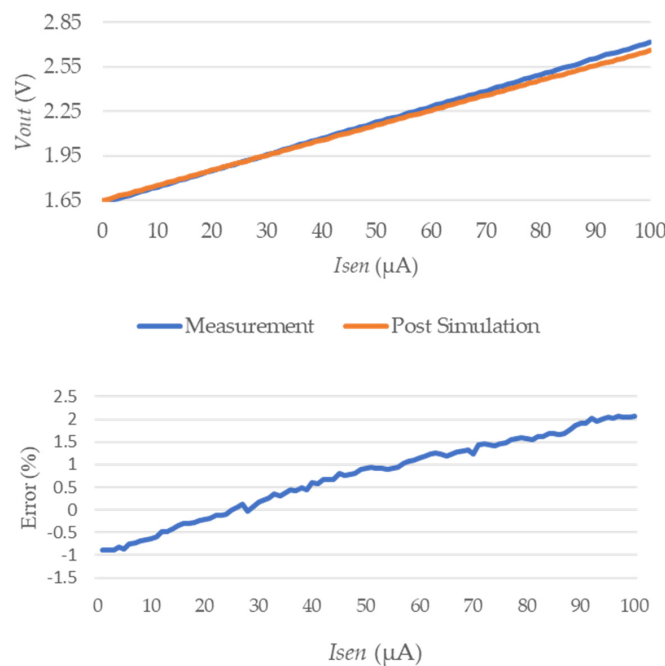


Figure 12. Firmware flowchart embedded in the Microcontroller Unit (MCU).



(a)

Figure 13. Cont.

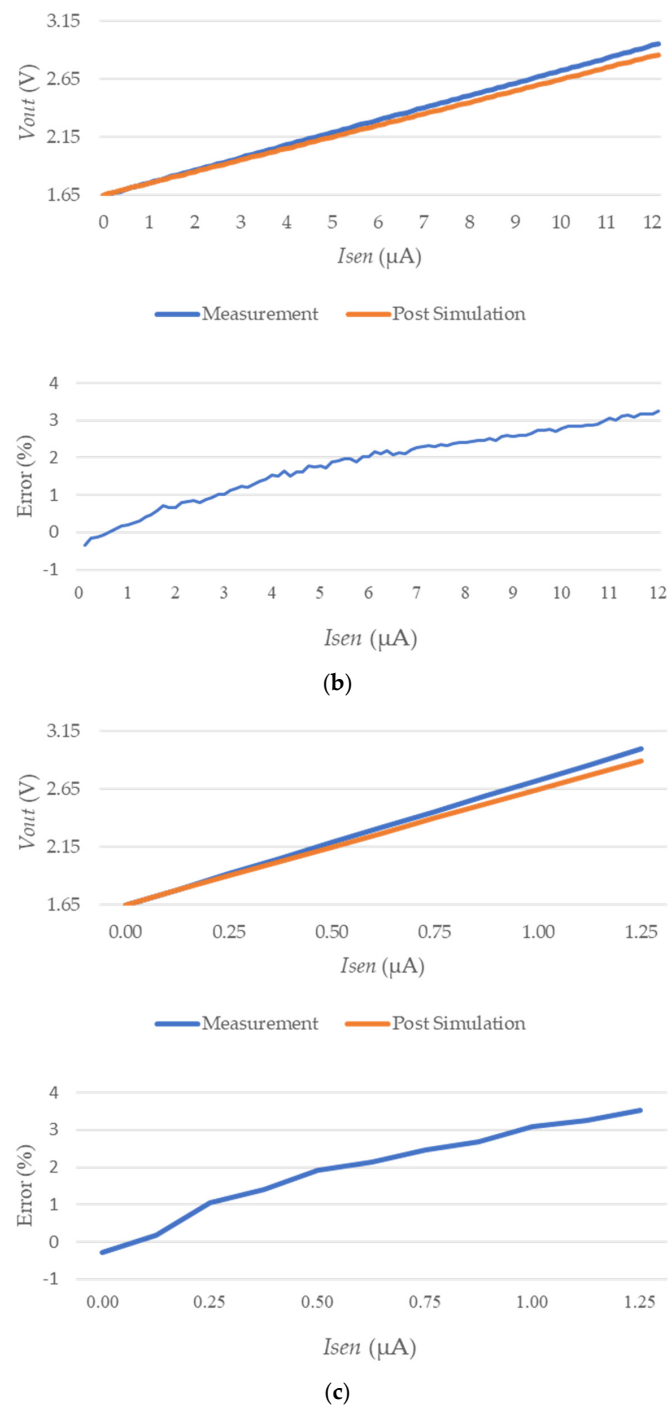


Figure 13. Comparison graphs of V_{out} versus I_{sen} and error between the measurement result and post simulation result when (a) $R_f = 10\text{ K}\Omega$; (b) $R_f = 100\text{ K}\Omega$; and (c) $R_f = 1\text{ M}\Omega$.

Table 2. Extracted I_{sen} and error rates with the conventional TIA and proposed TIA.

Expected I_{sen} (A)	Measured I_{sen} with Conventional TIA (A)	Measured I_{sen} with Proposed TIA (A)	Error Rate of Conventional TIA (%)	Error Rate of Proposed TIA (%)
100 μ	100.48 μ	100.48 μ	0.48	0.48
10 μ	13.32 μ	10.069 μ	33.278	0.698
1 μ	2.253 μ	1.005 μ	125.3	0.5

A comparison of the proposed readout with existing variable gain TIA architectures is presented in Table 3. Although a wide dynamic range is achieved by the TIA in several architectures, these solutions cannot achieve a linear output across the entire dynamic range. In contrast, the presented TIA showed good linearity throughout the targeted dynamic range, providing a relatively acceptable range. Furthermore, the proposed readout circuit is accomplished by a low power consumption of 0.38 mW and a small area of 0.282 mm², which are important factors for wearable patch type healthcare devices.

Table 3. Comparison of the proposed readout with existing architectures.

Ref.	Input Current Range (A)	Input Dynamic Range (dB)	Power Consumption (mW)	Transimpedance Gain Range (dBΩ)	Supply Voltage (V)	Technology	Area mm ²	Error Rate (%)
Our work	0.1 μ–100 μ	60	0.38	60–120	3.3	0.18 μm CMOS	0.282	1
[26]	1 μ–2 m	66	21	54–100	3.3	0.18 μm CMOS	0.356	0.40
[31]	100 f–1 μ	140	10.3	N/A	1.8	0.18 μm CMOS	1.015	N/A
[32]	N/A	77	2.71	N/A	3.3	0.18 μm CMOS	1.21	N/A
[38]	4.21 p–369 n	98.9	0.5	138–168	1.5	0.35 μm CMOS	0.3	N/A

4. Conclusions

In this work, the readout circuit consisting of a digitally adjustable R-TIA is designed and fabricated in a 0.18 μm CMOS process for various sensors that have current output. The proposed readout circuit is designed to adopt multiple electrochemical sensors for multifunctional wearable healthcare devices. The auto-adjustable R-TIA is developed to cover a wide range of I_{sen} by algorithm implemented in the MCU, which is altering the R_f value based on the current range. The R-TIA consists of the op-amp and feedback stage. As the R-TIA internal block, the two-stage op-amp is designed that is comprised of a bias stage, differential amplifier stage, and common source amplifier stage; it achieved a 97.5 dB gain and 64.05 degrees phase margin. To make the R_f adjustable, a resistor array with an 8×1 AMUX is embedded in the R-TIA circuit. The total area of the proposed readout circuit is 1030 μm × 620 μm, including the pads, and its power consumption is 0.38 mW with a power supply of 3.3 V. The measurement result shows that the proposed circuit can cover a wide range of sensor current from 0.1 μA to 100 μA and has an error rate less than 1%.

Author Contributions: Conceptualization, H.P. and S.J.; methodology, H.P. and C.P.; software, H.P.; validation, H.P., S.L. and H.-J.C.; formal analysis, all authors; investigation, H.P. and S.L.; resources, S.J., C.P. and H.-J.C.; data curation, H.P. and S.L.; writing—original draft preparation, S.L.; writing—review and editing, H.P., S.L., S.J., C.P. and H.-J.C.; visualization, S.J.; supervision, S.J. and H.-J.C.; project administration, S.J. and H.-J.C.; funding acquisition, H.-J.C. All authors have read and agreed to the published version of the manuscript.

Funding: This research was supported by Kumoh National Institute of Technology (2018104115).

Data Availability Statement: The datasets generated from the current study are available from the corresponding author on reasonable request.

Conflicts of Interest: The authors declare no conflict of interest.

References

- Xie, J.; Chen, Q.; Shen, H.; Li, G. Review—Wearable Graphene Devices for Sensing. *J. Electrochem. Soc.* **2020**, *167*, 037541. [[CrossRef](#)]
- Sweeney, D.; Quinlan, L.R.; Browne, P.; Richardson, M.; Meskill, P.; ÓLaighin, G. A Technological Review of Wearable Cueing Devices Addressing Freezing of Gait in Parkinson’s Disease. *Sensors* **2019**, *19*, 1277. [[CrossRef](#)] [[PubMed](#)]
- Sana, F.; Isselbacher, E.M.; Singh, J.P.; Heist, E.K.; Pathik, B.; Armoundas, A.A. Wearable Devices for Ambulatory Cardiac Monitoring: JACC State-of-the-Art Review. *J. Am. Coll. Cardiol.* **2020**, *75*, 1582–1592. [[CrossRef](#)] [[PubMed](#)]
- Lutz, W.; Sanderson, W.; Scherbov, S. The coming acceleration of global population ageing. *Nature* **2008**, *451*, 716–719. [[CrossRef](#)]
- Dall, T.M.; Gallo, P.D.; Chakrabarti, R.; West, T.; Semilla, A.P.; Storm, M.V. An Aging Population And Growing Disease Burden Will Require A Large And Specialized Health Care Workforce By 2025. *Health Aff.* **2013**, *32*, 2013–2020. [[CrossRef](#)]

6. Awais, M.; Palmerini, L.; Bourke, A.K.; Ihlen, E.A.F.; Helbostad, J.L.; Chiari, L. Performance Evaluation of State of the Art Systems for Physical Activity Classification of Older Subjects Using Inertial Sensors in a Real Life Scenario: A Benchmark Study. *Sensors* **2016**, *16*, 2105. [[CrossRef](#)]
7. Vijayalakshmi, K.; Uma, S.; Bhuvanya, R.; Suresh, A. A demand for wearable devices in health care. *Int. J. Eng. Technol.* **2018**, *7*, 1. [[CrossRef](#)]
8. Engel, J.M.; Mehta, V.; Fogoros, R.; Chavan, A. Study of Arrhythmia Prevalence in NUVANT Mobile Cardiac Telemetry System Patients. In Proceedings of the 2012 Annual International Conference of the IEEE Engineering in Medicine and Biology Society, San Diego, CA, USA, 28 August–1 September 2012; pp. 2440–2443.
9. Barrett, P.M.; Komatireddy, R.; Haaser, S.; Topol, S.; Sheard, J.; Encinas, J.; Fought, A.J.; Topol, E.J. Comparison of 24-h Holter Monitoring with 14-day Novel Adhesive Patch Electrocardiographic Monitoring. *Am. J. Med.* **2014**, *127*, 95.e11–95.e17. [[CrossRef](#)]
10. Altini, M.; Casale, P.; Penders, J.; ten Velde, G.; Plasqui, G.; Amft, O. Cardiorespiratory fitness estimation using wearable sensors: Laboratory and free-living analysis of context-specific submaximal heart rates. *J. Appl. Physiol.* **2016**, *120*, 1082–1096. [[CrossRef](#)]
11. Digiglio, P.; Li, R.; Wang, W.; Pan, T. Microflotronic Arterial Tonometry for Continuous Wearable Non-Invasive Hemodynamic Monitoring. *Ann. Biomed. Eng.* **2014**, *42*, 2278–2288. [[CrossRef](#)]
12. Etemadi, M.; Inan, O.T. Wearable ballistocardiogram and seismocardiogram systems for health and performance. *J. Appl. Physiol.* **2017**, *124*, 452–461. [[CrossRef](#)] [[PubMed](#)]
13. Lau, J.K.; Lowres, N.; Neubeck, L.; Brieger, D.B.; Sy, R.W.; Galloway, C.D.; Albert, D.E.; Freedman, S.B. iPhone ECG application for community screening to detect silent atrial fibrillation: A novel technology to prevent stroke. *Int. J. Cardiol.* **2013**, *165*, 193–194. [[CrossRef](#)] [[PubMed](#)]
14. Sohn, K.; Merchant, F.M.; Abohashem, S.; Kulkarni, K.; Singh, J.P.; Heist, E.K.; Owen, C.; Roberts, J.D., Jr.; Isselbacher, E.M.; Sana, F.; et al. Utility of a smartphone based system (cvrphone) to accurately determine apneic events from electrocardiographic signals. *PLoS ONE* **2019**, *14*, e0217217. [[CrossRef](#)] [[PubMed](#)]
15. Yoon, S.; Sim, J.K.; Cho, Y.H. A Flexible and Wearable Human Stress Monitoring Patch. *Sci. Rep.* **2016**, *6*, 23468. [[CrossRef](#)]
16. Lakshminarayana, S.; Park, Y.; Park, H.; Jung, S. High Density Resistive Array Readout System for Wearable Electronics. *Sensors* **2022**, *22*, 1878. [[CrossRef](#)]
17. Sempionatto, J.R.; Lin, M.; Yin, L.; De la Paz, E.; Pei, K.; Sonsa-Ard, T.; de Loyola Silva, A.N.; Khorshed, A.A.; Zhang, F.; Tostado, N.; et al. An epidermal patch for the simultaneous monitoring of haemodynamic and metabolic biomarkers. *Nat. Biomed. Eng.* **2021**, *5*, 737–748. [[CrossRef](#)]
18. Li, X.; He, L.; Li, Y.; Chao, M.; Li, M.; Wan, P.; Zhang, L. Correction to “Healable, Degradable and Conductive MXene Nanocomposite Hydrogel for Multifunctional Epidermal Sensor”. *ACS Nano* **2021**, *15*, 12453. [[CrossRef](#)]
19. Xi, W.; Yeo, J.C.; Yu, L.; Zhang, S.; Lim, C.T. Ultrathin and Wearable Microtubular Epidermal Sensor for Real-Time Physiological Pulse Monitoring. *Adv. Mater. Technol.* **2017**, *2*, 1700016. [[CrossRef](#)]
20. Yoon, S.; Yoon, H.; Zahed, M.A.; Park, C.; Kim, D.; Park, J.Y. Multifunctional hybrid skin patch for wearable smart healthcare applications. *Biosens. Bioelectron.* **2022**, *196*, 113685. [[CrossRef](#)]
21. Imani, S.; Bandonkar, A.J.; Mohan, A.M.V.; Kumar, R.; Yu, S.; Wang, J.; Mercier, P.P. A wearable chemical–electrophysiological hybrid biosensing system for real-time health and fitness monitoring. *Nat. Commun.* **2016**, *7*, 11650. [[CrossRef](#)]
22. Mariam El, G.; Fernández-García, R.; Ahyoud, S.; Gil, I. A Review of Flexible Wearable Antenna Sensors: Design, Fabrication Methods, and Applications. *Materials* **2020**, *13*, 3781.
23. Li, R.; Qi, H.; Ma, Y.; Deng, Y.; Liu, S.; Jie, Y.; Jing, J.; He, J.; Zhang, X.; Wheatley, L.; et al. A flexible and physically transient electrochemical sensor for real-time wireless nitric oxide monitoring. *Nat. Commun.* **2020**, *11*, 3207. [[CrossRef](#)] [[PubMed](#)]
24. Liu, J.; Lu, W.; Zhang, L.; Yang, J.; Yao, Z.-P.; He, Y.; Li, Y. Integrated hand-held electrochemical sensor for multicomponent detection in urine. *Biosens. Bioelectron.* **2021**, *193*, 113534. [[CrossRef](#)] [[PubMed](#)]
25. Pan, Y.; Zuo, J.; Hou, Z.; Huang, Y.; Huang, C. Preparation of Electrochemical Sensor Based on Zinc Oxide Nanoparticles for Simultaneous Determination of AA, DA, and UA. *Front. Chem.* **2020**, *8*, 2538. [[CrossRef](#)]
26. Ma, R.; Liu, M.; Zheng, H.; Zhu, Z. A 66-dB Linear Dynamic Range, 100-dB·Ω Transimpedance Gain TIA With High-Speed PDSH for LiDAR. *IEEE Trans. Instrum. Meas.* **2020**, *69*, 1020–1028. [[CrossRef](#)]
27. Micusik, D.; Zimmermann, H. 130dB-DR Transimpedance Amplifier with Monotonic Logarithmic Compression and High-Current Monitor. In Proceedings of the 2008 IEEE International Solid-State Circuits Conference—Digest of Technical Papers, San Francisco, CA, USA, 3–7 February 2008; pp. 78–597.
28. Mičušík, D.; Zimmermann, H. Transimpedance amplifier with 120 dB dynamic range. *Electron. Lett.* **2007**, *43*, 159–160. [[CrossRef](#)]
29. Aznar, F.; Gaberl, W.; Zimmermann, H. A highly sensitive 2.5 Gb/s transimpedance amplifier in CMOS technology. In Proceedings of the 2009 IEEE International Symposium on Circuits and Systems, Taipei, Taiwan, 24–27 May 2009; pp. 189–192.
30. Atef, M.; Hassan, O.; Awwad, F.; Khan, M.A.B. High Dynamic Range Photocurrent Sensory Circuit with a Multi-Transistor Background Light Cancellation Loop for Photoplethysmography Sensing. *Electronics* **2021**, *10*, 2769. [[CrossRef](#)]
31. Wang, W.; Sonkusale, S. An Approach for a Wide Dynamic Range Low-Noise Current Readout Circuit. *J. Low Power Electron. Appl.* **2020**, *10*, 23. [[CrossRef](#)]
32. Rad, R.E.; Hejazi, A.; Asl, S.-A.H.; Shehzad, K.; Verma, D.; Kim, S.; Rikan, B.S.; Pu, Y.; Kim, J.T.; Hwang, K.C.; et al. A 77-dB Dynamic-Range Analog Front-End for Fine-Dust Detection Systems with Dual-Mode Ultra-Low Noise TIA. *Sensors* **2021**, *21*, 6360. [[CrossRef](#)]

33. Hsu, C.; Hall, D.A. A current-measurement front-end with 160dB dynamic range and 7ppm INL. In Proceedings of the 2018 IEEE International Solid—State Circuits Conference—(ISSCC), San Francisco, CA, USA, 11–15 February 2018; pp. 326–328.
34. Dai, S.; Perera, R.T.; Yang, Z.; Rosenstein, J.K. A 155-dB Dynamic Range Current Measurement Front End for Electrochemical Biosensing. *IEEE Trans. Biomed. Circuits Syst.* **2016**, *10*, 935–944. [[CrossRef](#)]
35. Ferrari, G.; Gozzini, F.; Molari, A.; Sampietro, M. Transimpedance Amplifier for High Sensitivity Current Measurements on Nanodevices. *IEEE J. Solid-State Circuits* **2009**, *44*, 1609–1616. [[CrossRef](#)]
36. Hsu, C.L.; Jiang, H.; Venkatesh, A.G.; Hall, D.A. A Hybrid Semi-Digital Transimpedance Amplifier with Noise Cancellation Technique for Nanopore-Based DNA Sequencing. *IEEE Trans. Biomed. Circuits Syst.* **2015**, *9*, 652–661. [[CrossRef](#)] [[PubMed](#)]
37. Goldstein, B.; Kim, D.; Rottigni, A.; Xu, J.; Vanderlick, T.K.; Culurciello, E. CMOS low current measurement system for biomedical applications. *IEEE Trans. Biomed. Circuits Syst.* **2012**, *6*, 1017–1020. [[CrossRef](#)] [[PubMed](#)]
38. Kim, J.; Maitra, R.; Pedrotti, K.D.; Dunbar, W.B. A Patch-Clamp ASIC for Nanopore-Based DNA Analysis. *IEEE Trans. Biomed. Circuits Syst.* **2013**, *7*, 285–295. [[CrossRef](#)]
39. Lu, J.; Holleman, J. A Wideband Ultra-Low-Current On-Chip Ammeter. In Proceedings of the IEEE 2012 Custom Integrated Circuits Conference, San Jose, CA, USA, 9–12 September 2012; pp. 1–4.
40. Bennati, M.; Thei, F.; Rossi, M.; Crescentini, M.; Avino, G.D.; Baschiroto, A.; Tartagni, M. 20.5 A Sub-pA $\Delta\Sigma$ Current Amplifier for Single-Molecule Nanosensors. In Proceedings of the 2009 IEEE International Solid-State Circuits Conference—Digest of Technical Papers, San Francisco, CA, USA, 8–12 February 2009; pp. 348–349, 349a.
41. Crescentini, M.; Thei, F.; Bennati, M.; Saha, S.; de Planque, M.R.; Morgan, H.; Tartagni, M. A Distributed Amplifier System for Bilayer Lipid Membrane (BLM) Arrays With Noise and Individual Offset Cancellation. *IEEE Trans. Biomed. Circuits Syst.* **2015**, *9*, 334–344. [[CrossRef](#)]
42. Qiao, H. Design of a CMOS Two-stage Fully Differential Operation Amplifier. *J. Phys. Conf. Ser.* **2020**, *1449*, 012084. [[CrossRef](#)]
43. Ciofi, C.; Crupi, F.; Pace, C.; Scandurra, G.; Patane, M. A New Circuit Topology for the Realization of Very Low-Noise Wide-Bandwidth Transimpedance Amplifier. *IEEE Trans. Instrum. Meas.* **2007**, *56*, 1626–1631. [[CrossRef](#)]
44. Chuah, J.H.; Holburn, D. Design of Low-Noise High-Gain CMOS Transimpedance Amplifier for Intelligent Sensing of Secondary Electrons. *IEEE Sens. J.* **2015**, *15*, 5997–6004. [[CrossRef](#)]
45. Säckinger, E. *Analysis and Design of Transimpedance Amplifiers for Optical Receivers*; John Wiley & Sons: Hoboken, NJ, USA, 2017; pp. 207–278. [[CrossRef](#)]
46. Zihong, L.; Chao, B.; Zhihua, W.; Chun, Z. Full Custom Design of a Two-Stage Fully Differential CMOS Amplifier with High Unity-Gain Bandwidth and Large Dynamic Range at Output. In Proceedings of the 48th Midwest Symposium on Circuits and Systems, Covington, KY, USA, 7–10 August 2005; Volume 982, pp. 984–987.
47. Ramirez-Angulo, J.; Sawant, M.S.; López-Martín, A.; Carvajal, R.G. Compact implementation of high-performance CMOS current mirror. *Electron. Lett.* **2005**, *41*, 570. [[CrossRef](#)]
48. Balestrieri, E.; Daponte, P.; Rapuano, S. A state of the art on ADC error compensation methods. *IEEE Trans. Instrum. Meas.* **2005**, *54*, 1388–1394. [[CrossRef](#)]